Title

Hardening in Tungsten Tetraboride with the Addition of Carbon, Zirconium, and Silicon: Intrinsic vs Extrinsic Effects

Authors

Akopov, Georgiy
Hu, Shanlin
Shumilov, Kirill D
et al.

Publication Date

2024

DOI

10.1021/acs.chemmater.3c03092

Hardening in Tungsten Tetraboride with the Addition of Carbon and Zirconium: Intrinsic vs Extrinsic Effects

Georgiy Akopov,[1] Shanlin Hu,[2] Kirill Shumilov,[2] Spencer G. Hamilton,[2] Lisa E. Pangilinan,[2] Zerina Mehmedovic,[2] Hang Yin,[2] Paul J. Robinson,[2,3] Inwhan Roh,[2,4] Abby Kavner,[2] Anastassia N. Alexandrova,[2,5] Sarah H. Tolbert[2,5,6*] and Richard B. Kaner[2,5,6*]*

[1]*Department of Chemistry, Rutgers University-Newark, Newark, NJ 07102, USA*

[2]*Department of Chemistry and Biochemistry, University of California, Los Angeles (UCLA), Los Angeles, CA 90095, USA*

[3]*Department of Chemistry, Columbia University, New York, NY 10027, USA*

[4]*College of Chemistry, University of California, Berkeley, Berkeley, CA 94720, USA*

[5]*Department of Materials Science and Engineering, University of California, Los Angeles (UCLA), Los Angeles, CA 90095, USA*

[6]*California NanoSystems Institute (CNSI), University of California, Los Angeles (UCLA), Los Angeles, CA 90095, USA*

*Corresponding authors: ana@chem.ucla.edu, tolbert@chem.ucla.edu and kaner@chem.ucla.edu

Abstract

Alloys of tungsten tetraboride (WB_4) with the addition of C and Si were prepared by arc-melting of the constituent elements. The phase purity was established by PXRD and SEM/EDS analysis. Vickers hardness measurements showed hardness enhancement for alloys with a nominal composition of $(W_{0.98}Si_{0.02})$:11.6B and $(W_{0.95}C_{0.05})$:11.6B of 52.2 ± 3.0 and 50.5 ± 2.5 GPa

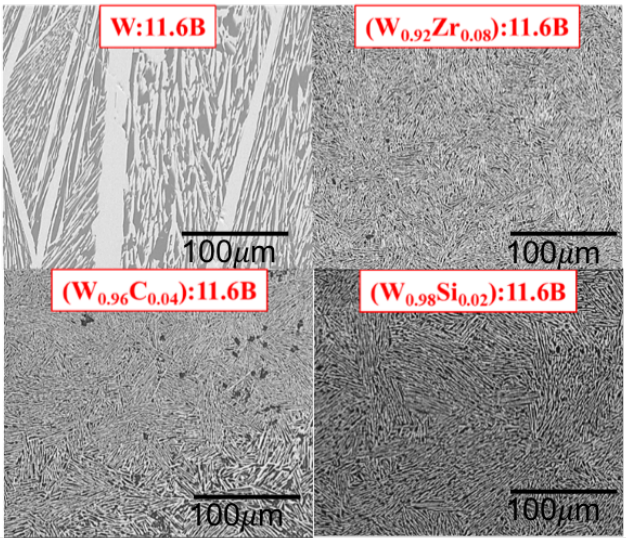

compared to 41.2 ± 1.4 GPa for pure WB_4. $(W_{0.92}Zr_{0.08})$:11.6B was determined in previous work to have a hardness of 55.9 ± 2.8 GPa. Bulk moduli were calculated following analysis of high-pressure radial diffraction data and were determined to be 329 ± 4 ($K0$' = 2) and 390 ± 9 ($K0$' = 0.6) GPa, for 8 at. % Zr and 5 at. % C-doping, respectively, compared to 326-339 GPa for pure WB_4. Computational analysis was used to determine the dopant positions in the crystal structure, and it was found that Zr primarily substitutes W in the 2c position, Si substitutes for the entire B3 trimers and C inserts in the B_{hex}-layer. The hardness enhancement in the case of Zr-doping is attributed primarily to extrinsic hardness effects (nanograin morphology), in the case of C - to intrinsic effects (interlayer bond strengthening), and in the intermediate case of Si - to both intrinsic and extrinsic effects (bond strengthening and fine surface morphology).

Keywords: *superhard, ultra-incompressible, transition metal borides, solid-solution, radial diffraction, elastic and plastic deformation*

Introduction

Transition metal borides possess a large variety of crystal structures,[1] which results in the ability to tune many useful materials characteristics, including their electronic, magnetic, optical, thermal, and mechanical properties.[1–7] The most commonly used mechanical property is hardness, and, as a consequence, superhard materials (possessing a Vickers hardness of greater than 40 GPa) and ultra-incompressible materials (possessing a bulk modulus greater than 300 GPa) have become increasingly popular subjects for research.[8–11]

Diamond, the hardest naturally occurring material, is expensive and cannot be readily used in processing of iron-containing alloys due to the formation of iron carbide. Cubic boron nitride, the second hardest material, requires high-pressure and high temperature to synthesize its hard polymorph. Boron carbide, the third hardest material, has a similar disadvantage as diamond in the

cutting of iron, as well as an expensive manufacturing process. Transition metal borides are thus interesting alternatives as more cost effective and easily synthesizable superhard materials.

In the last decade, the field of metal borides has seen a host of phases, their alloys and solid solutions: ReB_2 (the first reported superhard metal boride),[8,9] $W_{1-x}Ta_xB$ (having an enhanced bulk modulus compared to WB),[11,12] tungsten tetraboride (providing a cost-effective alternative to ReB_2),[13–18] metal dodecaborides (MB_{12})[19–22] (possessing true 3D networks of boron atoms) and ternary metal borides (featuring complex atomic arrangements).[23] The hardness of these metal borides can be enhanced through both intrinsic and extrinsic hardening effects. Intrinsic hardness generally involves solid-solution formation and novel chemical bonding effects, while extrinsic hardness is governed by surface grain hardening (Hall-Petch), patterning, and nano-size effects.[24]

WB_4 is an incongruently melting phase traditionally synthesized with excess boron (W:B ≈ 1:12), as this suppresses the formation of the softer tungsten diboride (WB_2, *P6₃/mmc*). However, the formation of WB_4 through the use of excess boron is accompanied by crystalline β-rhombohedral boron ($R\bar{3}m$).[10,14,25] Due to the presence of the two phases (WB_4 and β-rhombohedral boron), it is possible to control the size and shape of the grains and as a result influence bulk mechanical properties through extrinsic effects.[14,17] Alternatively, by substituting some of the tungsten atoms with tantalum, it is possible to stabilize

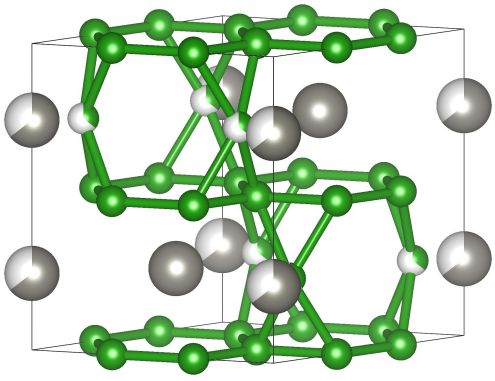

FIG. 1. Crystal structure of WB_4 with the *P6₃/mmc* space group (ICSD – Inorganic Crystal Structure Database – 291124).[51] Tungsten atoms are shown in gray, while boron atoms are in green; partially occupied positions are depicted by half-filled atoms.

the WB_4 structure at near-stoichiometric amounts of boron, with a nominal composition of $(W_{0.67}Ta_{0.33})$:4.5B.[18]

Tungsten tetraboride (WB_4, *P6₃/mmc*) has a unique structure among borides that contains partially filled metal and boron sites as well as voids (**FIG. 1**). This defect structure enables WB_4 to host both substitutional and interstitial dopants in voids and partial occupancy sites.[13–15,17] The addition of dopants leads to an enhancement of hardness. The hardening appears to be intrinsic in the case of Ta, Mo, Ti and Hf,[13–15] and some combination of intrinsic and extrinsic effects in the case of Zr, Y, Sc and some lanthanides.[14,17]

In the current study, we investigated the effects of adding carbon and silicon on the mechanical properties of WB_4. It was found that both elements have a similar effect on surface morphology to the addition of zirconium studied previously.[14] Tungsten tetraboride (WB_4) has a pseudo-cage structure that consists of alternating hexagonal layers of boron and tungsten with some partially occupied tungsten sites. Boron trimers sitting at those unoccupied sites combine with the boron layers to form "hourglass" structures; when the boron trimers above and below the boron layer correlate, they form distorted cuboctahedral cages. Therefore, WB_4 is able to accommodate dopants by either substitutional or interstitial doping into the partially filled metal and boron sites or into the voids. The defect structure allows the hardness of WB_4 to be tuned by doping with other transition metals, such as tantalum (Ta), manganese (Mn), and chromium (Cr).[16] However, little is known about the dopant positions in the WB_4 cage structure. Our goal here is to use a combination of high-pressure studies and computational chemistry to understand the mechanisms for enhanced hardness upon doping WB_4 with boron-like light elements (C and Si) as well as with transition metals (Zr) and whether the enhancement is intrinsic or extrinsic (or some combination of both) in nature.

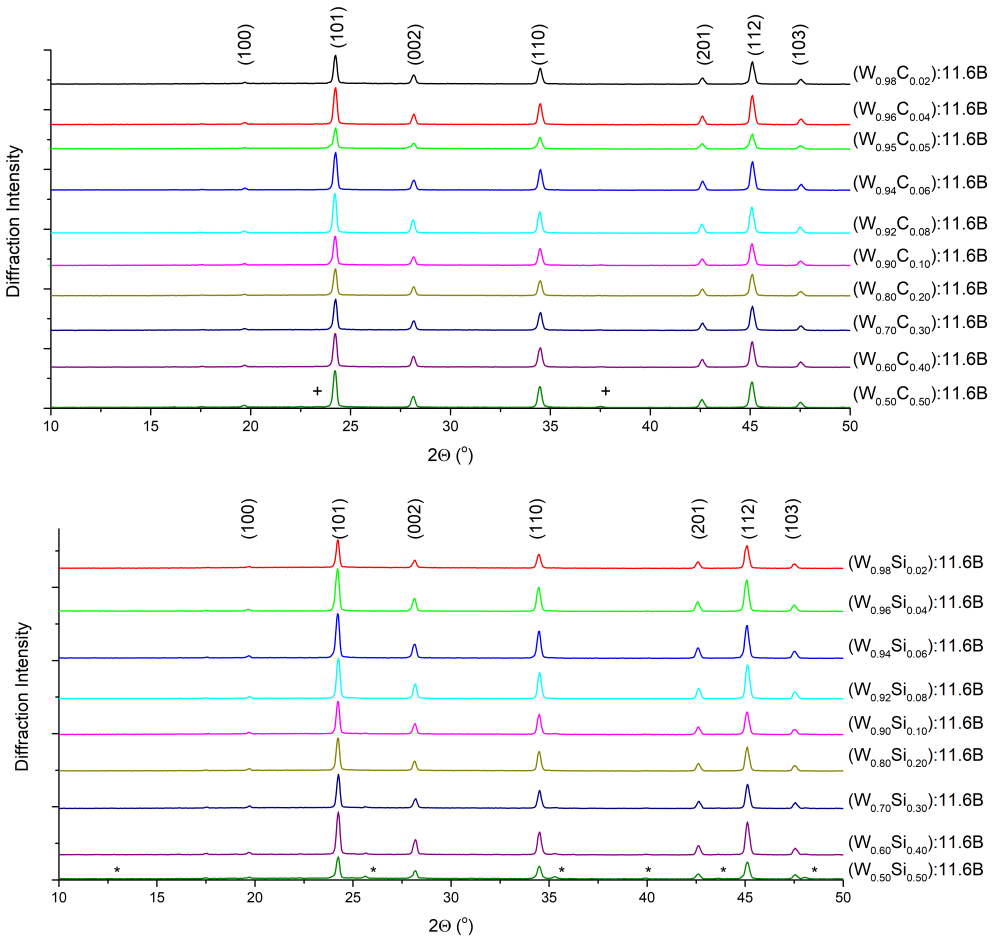

FIG. 2. Powder XRD patterns (10–50° 2Θ) of alloys of nominal composition **(top)** $(W_{1-x}C_x)$:11.6B and **(bottom)** $(W_{1-x}Si_x)$:11.6B. WB_4 (*P6₃/mmc*, JCPDS 00-019-1373) is present at all concentrations of C and Si. Peaks corresponding to a boron carbide phase (denoted by (+), $R\bar{3}m$, JCPDS 00-035-0798) can be observed at heavy concentrations of carbon addition. Peaks corresponding to WB_2 (denoted by (*), *P6₃/mmc*, JCPDS 01-073-1244)) can be observed at heavy concentrations of silicon addition.

Results and discussion

FIG. 2 and FIG. S1 show the powder X-ray diffraction data for alloys with nominal compositions of $(W_{1-x}C_x)$:4.5B, $(W_{1-x}Si_x)$:4.5B, $(W_{1-x}C_x)$:11.6B and $(W_{1-x}Si_x)$:11.6B. For the first two cases, the main WB_4 phase is accompanied by the lower boride phase (WB_2) at all concentrations of carbon and silicon addition. This can be explained by the fact that at 1:4.5 metal to boron ratio, the liquid peritectically decomposes into WB_4 and WB_2 upon cooling.[18,25,49] This further suggests that neither carbon nor silicon stabilize the WB_4 phase without the formation of

the lower boride, which suggests that they do not substitute for the tungsten positions in the structure, being non-metals by nature. For the second two cases, the main WB_4 phase is present, while the lower boride is absent, due to the stoichiometry used. At a metal to boron ratio of 1:11.6, the liquid peritectically decomposes upon cooling to form WB_4 and crystalline β-rhombohedral boron.[49–51] For both carbon and silicon at high concentrations, the powder diffraction data indicates the formation of insoluble impurities, suggesting a clear solubility limit.[13–15,17,18] Secondary phases can be seen in all four cases at high addition fractions, and more prominently in the case of added carbon, where with increasing concentration, peaks corresponding to boron carbide can be seen. This is further corroborated by the changes in lattice parameters *a* and *c* for the alloys of WB_4 with carbon and silicon prepared at 1:4.5 and 1:11.6 metal to boron ratios (**FIG. 3**). The lattice parameters do not change dramatically with the increasing concentration of carbon and silicon, from which we can deduce that neither of these elements substitute for tungsten in any significant amounts. They can, however, substitute for the partially occupied boron atoms in the WB_4 structure.[51]

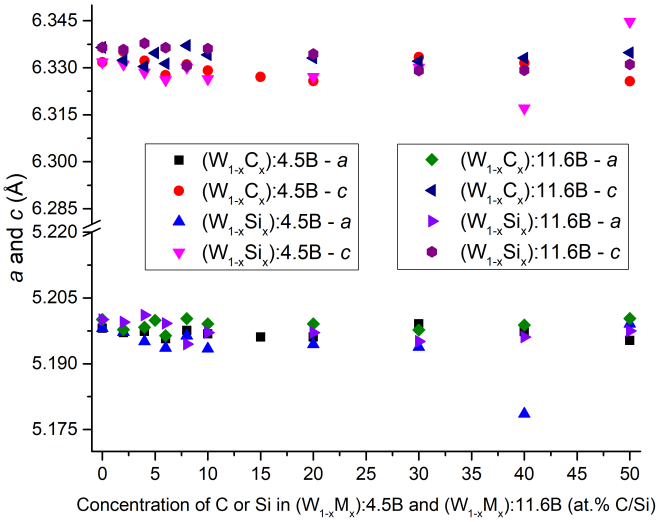

FIG. 3. Unit cell parameters *a* and *c* for alloys of WB_4 with C and Si, prepared at a nominal metal to boron composition of 1 to 4.5 and 1 to 11.6, calculated using *Maud*.[26–30] The literature value for the unit cell parameters of WB_4 are: $a = 5.1998(15)$, $c = 6.3299(19)$.[51]

To identify the preferred positions of Zr, C, and Si impurities, and corroborate the experimental observations, we used DFT calculations. First, we computationally identified the most stable realization of $WB_{4.2}$ with

respect to the B_3-trimer distribution. Next, that structure was used to compute the placement and formation enthalpies of the doped materials.

The $WB_{4.2}$ unit cell structure with unit *P6/mmc* symmetry was taken as the foundation for the calculations.[51] However, it was shown by Lech *et al*. that the crystal structure of $WB_{4.2}$ is disordered with a ~2/3 chance of a B_3-trimer substituting a W-atom in the Wyckoff 2(b) position. Therefore, to account for fractional occupancy sites, a 3×2×1-supercell was chosen, since it is the smallest supercell that guarantees an integer number - four - of B_3-trimers in the structure. Within this supercell, a set of structures was sampled, including but not limited to, structures of high symmetry, high bulk modulus, low energy, etc. (**FIG. S10**). The structure shown in **FIG. 4** is the one on which we focus the discussion, as it is the structure with not only the highest symmetry, *Cmcm*, but also the highest calculated bulk modulus (B_0 = ~293 GPa). Furthermore, the *Cmcm* structure was found to be the most stable at finite temperature with inclusion of configurational entropy.[43]

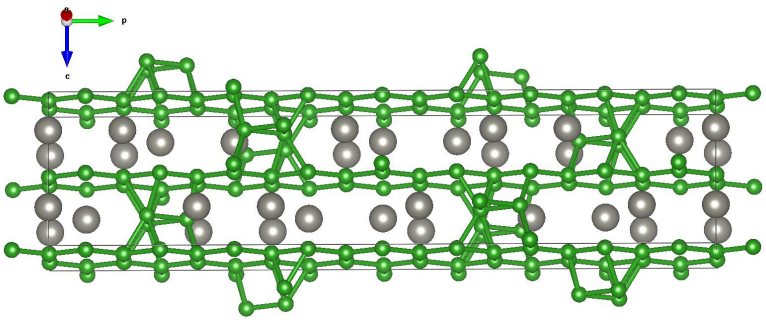

FIG. 4. Model *Cmcm* structure. A characteristic feature of this structure is alternating "rows" of B_3-trimers, "piercing" the material along the *a*-axis.

To identify the preferred positions of C, Si, Zr in the structure shown in **FIG. 4**, the formation enthalpies, H_0, were calculated (**Table 1**). By this metric, the preferential position for C is in the B_{hex}-layer in the [001] plane, in agreement with the hypothesis derived from the experiment. Si preferentially substitutes the entire B_3-trimer. Zr substitutes W in the Wyckoff 2(c) position (next to the edge of the B_3-trimer), and there is an only slightly less preferred structure where Zr

substitutes for W in the Wyckoff 2(c) position (next to the vertex of the B_3-trimer). Indeed, *ab initio* DFT calculations support experimental findings regarding the location of impurities within $WB_{4.2}$.

Table 1. Calculated Thermodynamic and Mechanical Properties of Model Structures

Impurity	Atoms Substituted	B_0,* GPa	H_0,# eV
Pure material	N/A	292.7	-12.6
C	Two B atoms in B_{hex}-layer above B_3-trimers	292.1	-8.7
	Four B atoms in B_{hex}-layer above B_3-trimers	289.8	-5.1
	One B atom in B_3-trimer	288.6	-7.3
Si	Two B atoms in B_{hex}-layer above B_3-trimer	274.9	-6.9
	One B atom in B_3-trimer	280.5	-9.2
	B_3-trimer	281.7	-10.4
Zr	W-occupancy	295.3	-12.9
	W-vacancy	292.0	-12.8

*B_0 = bulk modulus

#H_0 = formation enthalpy

The DFT calculations make it clear that C, Si, and Zr can substitute into the $WB_{4.2}$ lattice, resulting in intrinsic changes to the material's hardness. These intrinsic effects do not preclude additional extrinsic effects based on changes in grain structure, and so in addition to diffraction and computation studies, we examined the grain morphology of a range of carbon-doped WB_4 alloy compounds. **FIG. 5 and S2** show the SEM images of the surface of the alloys of WB_4 with carbon and silicon. In the case of a 1:4.5 metal to boron ratio, both carbon and silicon result in

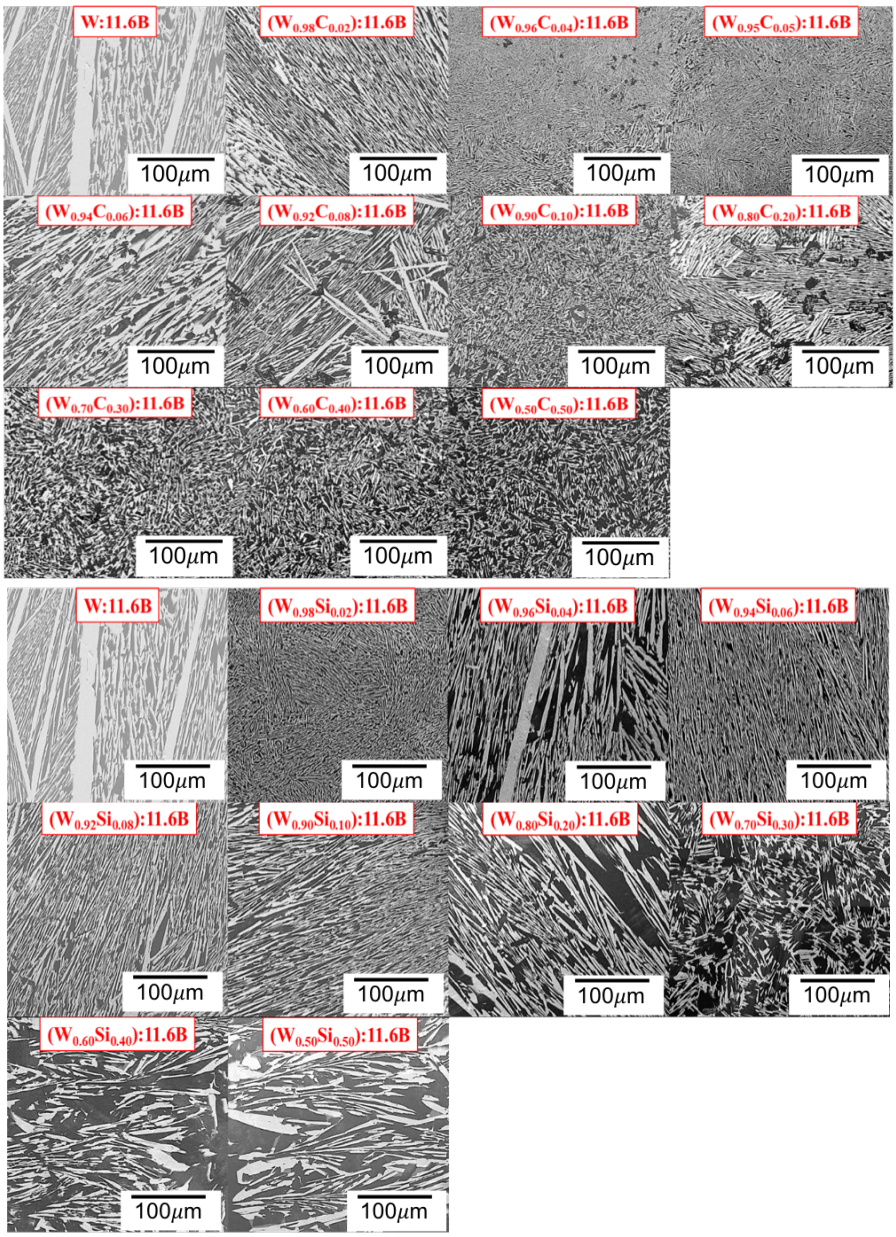

FIG. 5. SEM images for alloys of WB_4 with a nominal composition of **(top)** $(W_{1-x}C_x)$:11.6B and **(bottom)** $(W_{1-x}Si_x)$:11.6B showing a change in surface morphology associated with the effects of carbon and silicon and secondary phase formation. All SEM images were taken at 1000× magnification; the scale bars are 100 μm.

reduced grain sizes at low concentration, primarily manifesting at 6–8 at.% addition for carbon and 8–10 at.% for silicon, attributed to the rapid cooling caused by their addition. At high amounts of carbon addition, areas corresponding to boron carbide formation can be seen (**FIG. S2**).

FIG. 6 and FIG. S5 are graphs showing Vickers hardness of the alloys. For $(W_{1-x}C_x)$:11.6B (**FIG. 6 top**), the hardness increase at 5 at.% C to 52.2 ± 3.0 GPa, compared to 41.2 ± 1 GPa for the pure phase, correlates with the formation of a fine grained morphology, but may also have an intrinsic component (**FIG. 5 top**), while the second increase at 50 at.% C to 51.8 ± 6.1 GPa

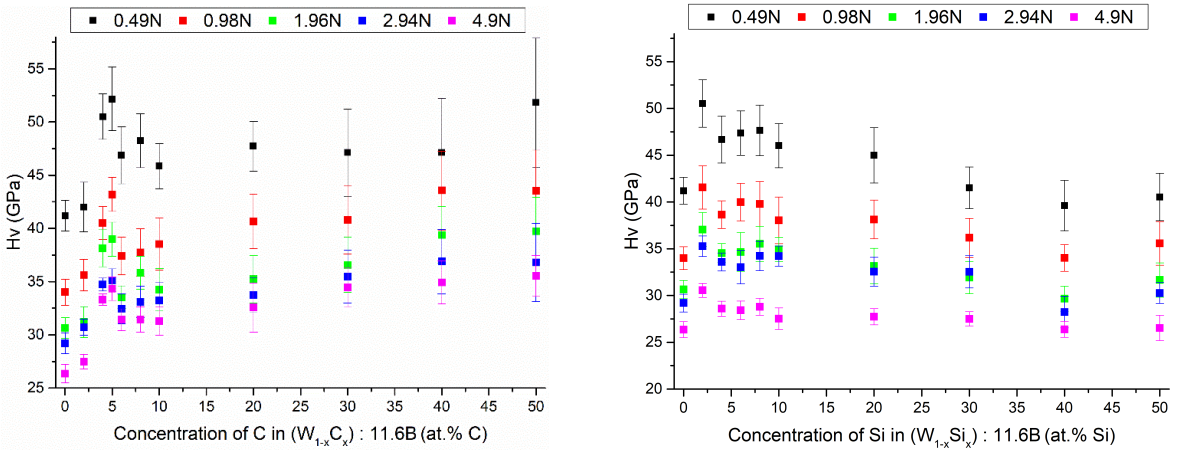

FIG. 6. Vickers micro-indentation hardness of alloys with a nominal composition of **(left)** $(W_{1-x}C_x)$:11.6B and **(right)** $(W_{1-x}Si_x)$:11.6B alloys at low (0.49 N) to high (4.9 N) loading.

appears to be the result of extrinsic effects due to the formation of boron carbide.[52] For $(W_{1-x}Si_x)$:11.6B (**FIG. 6 bottom**), the hardness maximum at 2 at.% Si of 50.5 ± 2.5 GPa again correlates with a changes in grain morphology (**FIG. 5 bottom panel**), while at higher amounts of silicon addition, the hardness plateaus at ~42 GPa. In the case of $(W_{1-x}C_x)$:4.5B (**FIG. S5 top**), similar trends are observed, but with lower absolute hardness values, where the hardness first increases to 38.0 ± 3.8 GPa at 6 at.% C, compared to 30.8 ± 2.8 GPa[18] for the pure phase, which correlates with changes in morphology and grain size (**FIG. S2 top panel**), while the second hardness increases to 53.4 ± 6.6 GPa at 50 at.% C clearly results from the formation of the

superhard boron carbide phase.[52] Similarly for $(W_{1-x}Si_x)$:4.5B (**FIG. S5 bottom**), the hardness maxima at 8–10 at.% Si of 38.7 ± 3.0 and 40.0 ± 2.2 GPa, respectively, correspond to changes in grain morphology (**FIG. S2 bottom panel**), while at higher amounts of silicon addition, the hardness plateaus at ~36 GPa.

To complement the pure addition of C, Si, and Zr to $WB_{4.2}$, a few more complex combinations were produced. Specifically, C was added to two WB_4 alloy compositions of interest: the single-phase alloy with a WB_4 structure prepared with a stoichiometric amount of boron – $(W_{0.67}Ta_{0.33})$:4.5B;[18] and an alloy with 8 at.% zirconium addition – $(W_{0.92}Zr_{0.08})$:11.6B[14] – which resulted in the most nano-structured grain morphology. In the case of $(W_{0.67}Ta_{0.33})$:4.5B, when carbon was added, a secondary lower boride (WB_2) started to form at about 20 at.% C, which can be explained by the fact that as boron carbide forms, it lowers the amount of available boron (**FIG. S3**). The grain morphology does not change drastically, until ~40 at.% carbon addition (**FIG. S4**), at which point, the boron carbide phase starts to generate a lamellar decomposition pattern.[53] In agreement with these observations, indentation data show only a gradual increase in hardness to a maximum of 44.6 ± 7.5 GPa at 100 at.% C addition, mainly due to the formation of boron carbide. No peaks in the hardness as a function of C addition are observed, as in the case of C or Si substituted into $WB_{4.2}$, suggesting only grain size and compositional effects are at play. By contrast, in the case of $(W_{0.92}Zr_{0.08})$:11.6B, the nano-morphology is lost immediately upon the addition of carbon, resulting in a hardness decreases from 55.9 ± 2.8 GPa[14] for the pure phase, to ~45 GPa with low carbon addition, and back up to 52.4 ± 6.9 GPa at 100 at.% C, again due to the formation of boron carbide (**FIG. S6**). For $(W_{0.92}Zr_{0.08})$:11.6B, lower borides (WB_2) do not form

until ~80 at.% C addition because of the large amount of excess boron (**FIG. S3**). These results make two things clear: (1) small compositional changes can produce dramatic morphological changes which can, in turn, dramatically change the bulk hardness of the composite through extrinsic effects, and (2) adding substituents like carbon can dramatically change the phase composition of a sample, resulting in a complex mixture of effects.

Because of the large number of possible combinations and the interplay of intrinsic and extrinsic effects, we chose three of the hardest phases for further study. The Vickers hardness values and grain morphologies of these three compositions – WB_4 with 8 at.% Zr, 5 at.% C, and 2 at.% Si – can be seen in **FIG. 7**. The metal and the two non-metals have a similar effect on the grain morphology, resulting in small grains for all substituted compositions. The key question is: to what extent is the increased hardness discussed above a result only of this decreased grain size, given that all elements have the potential to substitute into the host lattice?

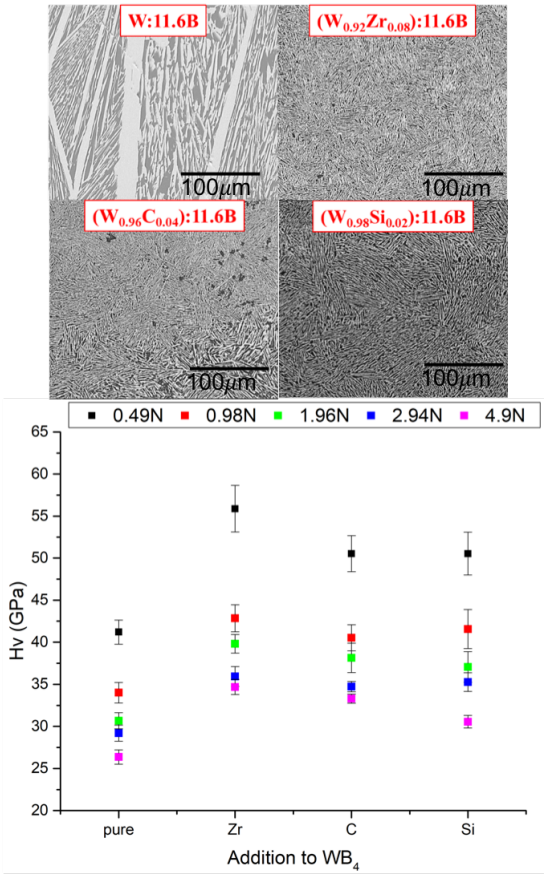

FIG. 7. Vickers micro-indentation hardness and SEM images of WB_4 alloys with a nominal composition of $(W_{1-x}M_x)$:11.6B, where M = zirconium (x = 0.08), carbon (x = 0.04) and silicon (x = 0.02) at low (0.49 N) to high (4.9 N) loading. All SEM images were taken at 1000x magnification; the scale bars are 100 μm.

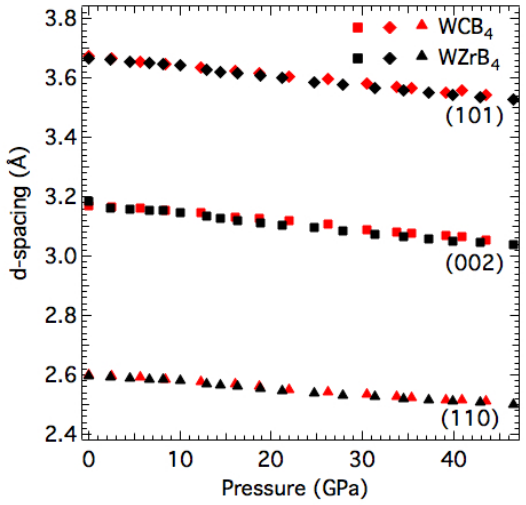

FIG. 8. Selected d spacings vs. pressure collected at φ = 54.7° for $W_{0.96}C_{0.04}B_4$ and $W_{0.92}Zr_{0.08}B_4$.

Although Vickers micro-indentation provides a direct measurement of a material's hardness, it often does not afford sufficient mechanical insight into intrinsic properties or explain the effects of dopant positions on the material's bonding motif. Our goal here is to use high-pressure studies to understand the mechanisms for tunable hardness from doping WB_4 with boron-like light elements (C and Si) as well as transition metals (Zr). Previously we have demonstrated that the WB_4 structure is stabilized by boron with a ratio of 1:11.6 and a small amount of secondary transition metal. Samples with nominal compositions of $(W_{0.96}C_{0.04})$:11.6B and $(W_{0.92}Zr_{0.08})$:11.6B, especially, exhibit the best homogeneity in morphologies, essentially single-phase WB_4 with remarkable hardness. For simplicity, we now abbreviate them as $W_{0.96}C_{0.04}B_4$ and $W_{0.92}Zr_{0.08}B_4$ to clarify the structure of the sample and the percentage of the dopants, ignoring the excess boron.

By compressing a sample under non-hydrostatic stress in a diamond anvil cell, radial X-ray diffraction can be readily collected at incremental pressure steps (up to 45 GPa) *in situ* to provide information about the evolution of the unit cell volume, and also lattice specific measurements of

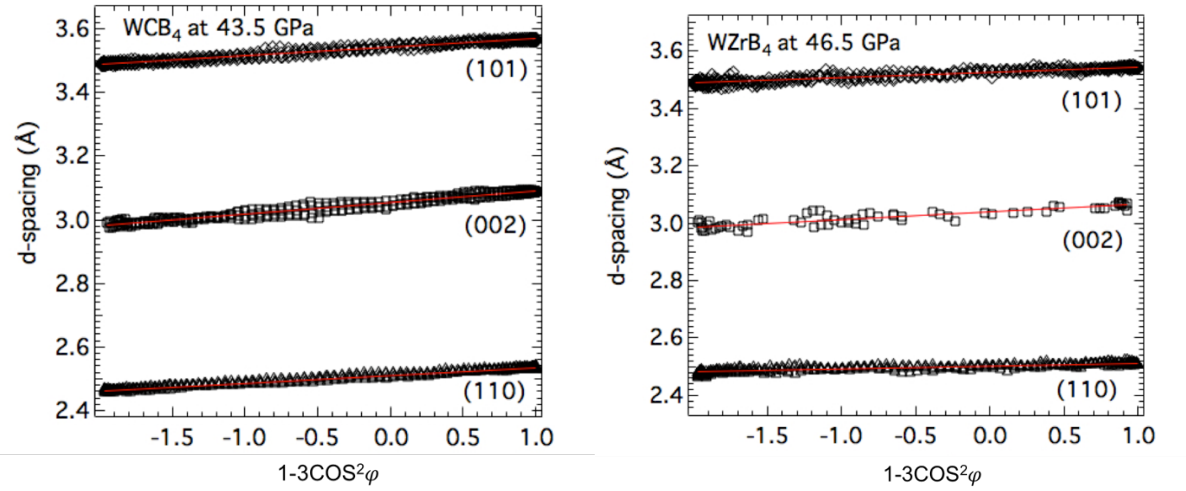

FIG. 9. Linearized plots of d spacings for $W_{0.96}C_{0.04}B_4$ (top) and $W_{0.92}Zr_{0.08}B_4$ (bottom) as a function of $(1\text{-}3\cos^2\varphi)$ at the highest pressure. Solid lines are the best linear fit to the data.

differential strain and predominant slip planes in the material. In the radial geometry, diffraction data is collected at a range of angles with respect to the low and high stress directions, and the stress state of the sample under non-hydrostatic compression can be determined according to lattice strain theory, as explained in **FIGS. S7-9**. The integrated "cake" patterns, azimuthal angle (η) versus diffraction angles (2θ) were reported at both low and high pressure. At low pressure, the nearly straight diffraction lines of the "cake" patterns are due to the hydrostatic stress state. However, at high pressure, sinusoidal variations of the diffraction lines occur due to nonhydrostatic stress, so that the diffraction lines deviate to higher angle (2θ) in the high stress direction ($\varphi = 0°$) and to lower angle (2θ) in the low stress direction ($\varphi = 90°$). The waviness of the diffraction lines indicates the lattice-supported strains, which will be further discussed in **FIG. 9**. In the 1-D diffraction patterns, a clear shift of the peaks obtained at $\varphi = 54.7°$ (the magic angle) to higher angles at higher pressure indicates a decrease in the lattice spacing with greater compression, and the peak broadening implies strain inhomogeneity. The pressure dependent d spacings of the (002), (101) and (110) planes at the quasi-hydrostatic condition ($\varphi = 54.7°$, magic angle), are plotted in

FIG. 8. Examples of the full description of the d-spacings at all angles are shown in **FIG. 9**, which demonstrate the linear correlation between d spacings and $(1-3\cos^2\varphi)$ for the selected planes of WB_4 solid solutions at the highest pressure. According to Equation (3), the slope of each line yields the corresponding *Q(hkl),* and the intercept gives the d spacing under quasi-hydrostatic compression. The differential strain *(t/G)*, which is the ratio of differential stress *(t)* to shear modulus *(G)*, can be directly determined from the *Q(hkl)* value, as shown in Equation (4). In **FIG. 10**, the *t(hkl)/G* ratio increases linearly with pressure at the beginning, then levels off, increases slowly, and eventually plateaus at 30 GPa. The plateau indicates the onset of plastic deformation, where the bonding starts to break and the lattice dislocations become irreversible. The planes with higher *t(hkl)/G* plateau value (differential strain) can be deformed to a greater extent before undergoing plastic deformation, and the plane with lowest *t(hkl)/G* plateau slips with the lowest deformation.

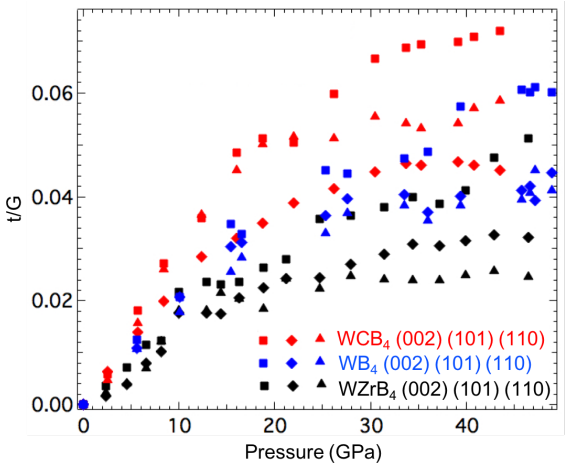

FIG. 10. The ratio of differential stress to shear modulus (t/G) for pure WB_4 (blue) compared to WB_4 with 8 at.% Zr (black) and 4 at.% C (red) addition.

As seen in **FIG. 10**, $W_{0.96}C_{0.04}B_4$ supports higher differential strain, *t(hkl)/G*, than pure WB_4 in all three lattice planes of choice, indicating lattice planes in $W_{0.96}C_{0.04}B_4$ can undergo more deformation before bond breaking and are less prone to slip than in pure WB_4. In other words, $W_{0.96}C_{0.04}B_4$ is intrinsically harder than WB_4. In $W_{0.96}C_{0.04}B_4$, the (002) plane, parallel to the layers of boron and tungsten atoms, supports the highest differential strain followed by the (110) plane and then the (101) plane. In pure WB_4, however, the (110) and (101) planes have almost identical differential strain. The fact that the (002) plane is greatly enhanced and the (110) plane is less

prone to slip than the (101) plane in $W_{0.96}C_{0.04}B_4$ suggests that the bonding in the c axis is particularly strengthened by doping with carbon and confirms the computational results that carbon substitution into the boron sheets right above the boron trimer, enhancing the C_{layer}-$B_{cluster}$ bonds (*vide infra*). This suggests that adding carbon maintains the cage structure and strengthens the cross-links between the interlayers, contributing to the enhanced intrinsic hardness of $W_{0.96}C_{0.04}B_4$.

When 8 at.% zirconium is doped into WB_4, the resultant solid solution is the hardest of any of the materials discussed here, but radial diffraction studies show decreased differential strain in the (002), (100) and (101) planes compared to pure WB_4 (**FIG. 10**). The decrease of the differential strain in all three lattice planes in $W_{0.92}Zr_{0.08}B_4$ suggests that the pseudo-cage structure of WB_4 is disrupted by doping with Zr. In addition, the weakening in the c axis is also observed from strain anisotropy that indicates that the (101) plane supports higher differential strain than the (110) plane in $W_{0.92}Zr_{0.08}B_4$. This is consistent with computational results that Zr weakens bonding between interlayers by doping into the tungsten vacancies. The fact that $W_{0.92}Zr_{0.08}B_4$ has the highest Vickers hardness among pure WB_4 and its solid solutions, but has lower plateau differential strain values for all lattice planes, suggests that the enhanced Vickers hardness by doping Zr largely results from improved extrinsic hardness due to the very small grain sizes found in this material. Vicker's hardness is sensitive to both intrinsic and extrinsic effects, while the high-pressure experiments explore only a material's microscopic deformation, which contributes to the intrinsic hardness.

The Si doped sample posed an experimental challenge because the highly elongated grains produced strong texture in the radial diffraction experiment, which resulted in insufficient data for some lattice planes to analyze the differential strain. As shown in **FIG. S9**, the Si doped sample

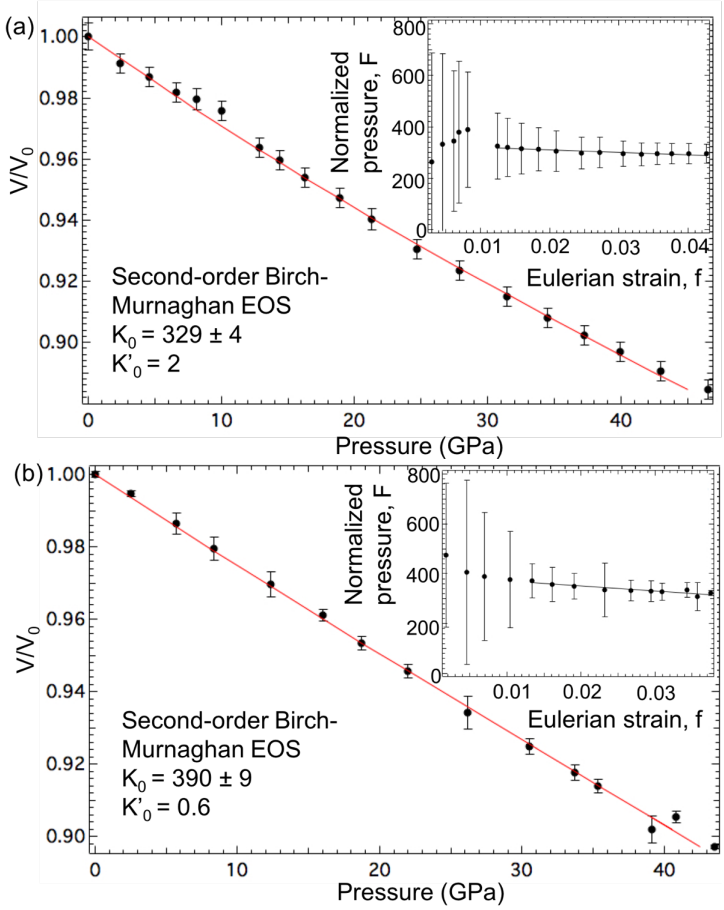

FIG. 11. Evolution of the unit cell volume for $W_{0.92}Zr_{0.08}B_4$ (**a**) and $W_{0.96}C_{0.04}B_4$ (**b**) as a function of pressure under nonhydrostatic compression. The volume was measured at $\varphi = 54.7°$. The red solid line is the best fit to the third-order Birch-Murnaghan equation-of-state (EOS). Inset is the third-order Birch-Murnaghan EOS plotted in terms of normalized pressure and Eulerian strain. The straight line in the inset plot yields the ambient pressure bulk modulus.

exhibits strong texture even at pressure as low as 1.7 GPa. The few lattice planes that could be analyzed are plotted in **FIG. S10**, along with the data for the undoped, C-doped, and Zr-doped material. While the quality of the data is fairly poor, it is clear that the differential strain is similar to or lower than that of the pure WB_4, indicating that, similar to the Zr doped case, the increase in hardness likely arises primarily from extrinsic effects.

The rigid cage structure along the *c*-direction in the WB_4 system not only supports a high differential strain, but also resists great hydrostatic compression (high bulk modulus). From fitting the third order Birch-Murnaghan equation-of-state in terms of normalized pressure and Eulerian strain, the bulk moduli for $W_{0.92}Zr_{0.08}B_4$ and $W_{0.96}C_{0.04}B_4$ were determined to be 329 ± 4 GPa ($K_0' = 2$) and 390 ± 9 GPa ($K_0' = 0.6$), respectively (**FIG. 11**). The bulk modulus of $W_{0.92}Zr_{0.08}B_4$ is within the range of the bulk modulus of WB_4 (326–339 GPa), and other borides,[54,55] while $W_{0.96}C_{0.04}B_4$ has a higher bulk

modulus than WB_4. This finding also implies that the cage structure is strengthened in $W_{0.96}C_{0.04}B_4$. An accurate bulk modulus for the Si-doped sample, unfortunately, could not be calculated.

To validate these conclusions, and clarify the effects of C, Zr, and Si dopants on the local rigid cage structure and its influence on the mechanical properties of the material, we return to theoretical calculations. First, bulk moduli, B_0, were calculated for structures with the impurities in several different positions (**Table 1**). DFT-based B_0 values are significantly underestimated compared to the experimental values. The discrepancy can be attributed to the use of a GGA functional (PBE), which suffer from delocalization error resulting in underestimated B_0 by ~9%;[56] poor treatment of Van der Waals interactions; and disregard for relativistic effects in W. We have attempted to recalculated the bulk modulus for pure and C-doped structures with HSE06[57,58] hybrid functionals, and observed an increase in B_0, but still not to the level of the experimental results. We therefore used PBE functional for its greater computational efficiency, and use DFT calculations for trends only. The inclusion of Si decreases the computed B_0 of $WB_{4.2}$, while the

inclusion of C leaves the computed B_0 practically unchanged. The introduction of Zr in either position marginally increases the computed B_0.

A better measure of mechanical hardness is the shear modulus. Accessing it computationally for such a large supercell is prohibitively expensive, and thus, we infer information about stability against shear through the analysis of electron density using eh Quantum Theory of Atoms in Molecules (QTAIM). QTAIM analyzes the topology of the quantum mechanical charge density, ρ. Specifically, ρ is rigorously partitioned into atomic basins, defined by zero-flux surfaces where the normal vector at any point on the surface is orthogonal to the gradient of the electron density ($\nabla\rho(\mathbf{r}) \cdot \mathbf{n}(\mathbf{r}) = 0$). There are 4 types of critical points (CPs) in ρ: nuclear, bond, ring, and cage CPs, defined by the curvature of $\rho(\mathbf{r})$ at that point. A bond CP (BCP), of most interest to this study, is a maximum in 2 spatial directions and a minimum in 1 spatial direction, a ring CP (RCP) is a maximum in 1 spatial direction and a minimum in 2 spatial directions, and a cage CP

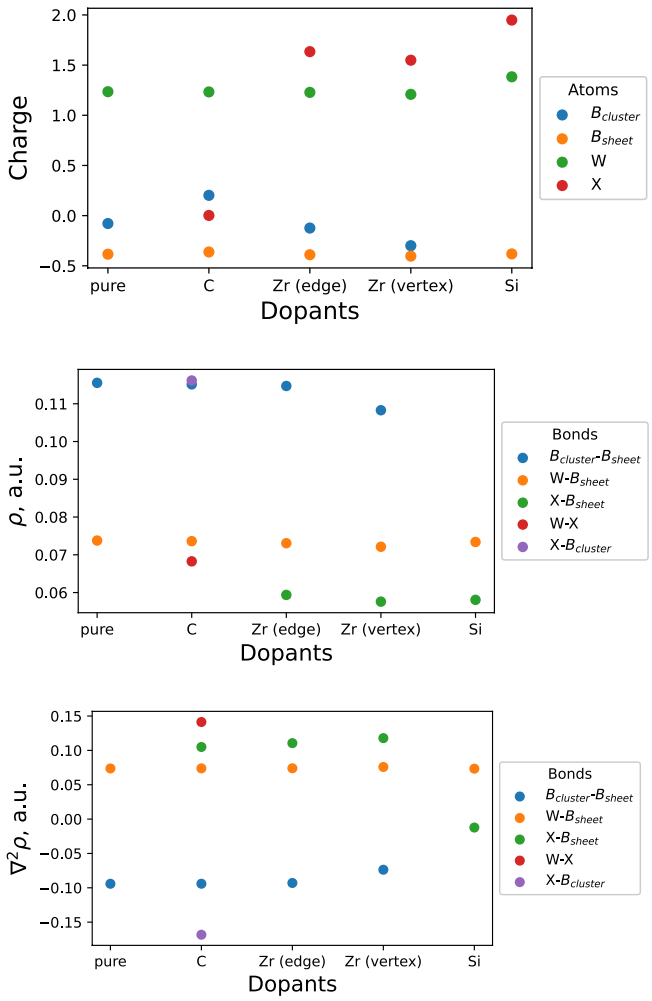

FIG. 12. QTAIM analysis of BCPs for model structures. (a) Average Bader atomic charges in model structures. (b) Average electron density at BCPs, connecting "layers" of the material. Average Laplacian at BCPs, connecting "layers" of the material.

(CCP) is a minimum in all 3 spatial directions. Topological quantities include curvature and $\nabla^2\rho(\mathbf{r})$. Characteristics of ρ at CPs are telling of materials properties, such as mechanical stability.

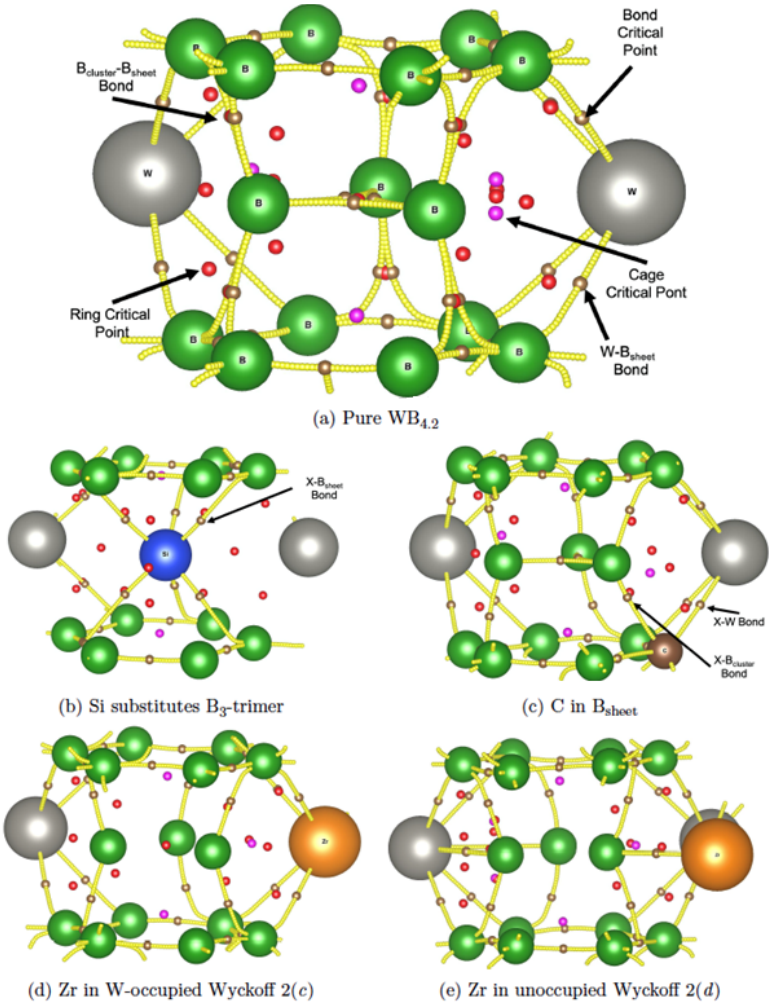

FIG. 13. Bonding QTAIM analysis of model structures with selected impurities. Point descriptions: Bond CPs—brown, Ring CPs—red, Cage CP— magenta. Lines of gold critical points depict bond paths.

Since chemical bonding is a local effect, and also the bonding is largely covalent in $WB_{4.2}$, we used a smaller 2×2×1-supercell with a single B_3-trimer, isolated from other trimers. The relevant QTAIM graphs are shown in **FIG. 12** and the BCPs discussed are shown in **FIG. 13**. Due to the pseudo-layered nature of the material, the weakest slip system in $WB_{4.2}$ is the shear in the [001] plane. Therefore, the bonds connecting hexagonal layers either through B_3-trimers or through metal atoms are essential for strengthening $WB_{4.2}$ against shear.

The strongest bond formed in the C-doped $WB_{4.2}$ is the 2-center bond between B in the B_3-trimer and C in the B_{hex}-layer (**FIG. 12**). It has the highest electron density and lowest Laplacian in the entire structure. The formation of the strong C_{layer}-$B_{cluster}$ bond is likely related to the resistance of the material to shear. The bonds formed with other impurities generally have lower electron density

and higher positive Laplacians, associated with bond weakening. For instance, the substitution of W with Zr in Wychoff 2c leaves the interlayer bonding unchanged or weakens it, while substitution of Zr in the W-vacancy always depletes the electron density of interlayer bonds (**Table 2**). This result is consistent with the experimental observation that the plateau differential strain observed through high pressure radial diffraction is actually lower in $W_{0.92}Zr_{0.08}B_4$ than in WB_4 .

An extreme example of bond weakening is Si, upon substituting itself for the entire B_3-cluster. The bonds it forms with the B-sheets are characterized by small $\rho(\vec{r})$ and near-zero $\nabla\rho(\vec{r})$). While the metal dopants generally slightly weaken $B_{cluster}$-B_{sheet} (lower in $\rho(\vec{r})$ and higher in $\nabla\rho(\vec{r})$), the Si impurity replaces those bonds with significantly weaker bonds. This may explain why the hardness is only slightly increased in Si-doped $WB_{4.2}$, despite a dramatic reduction in grain size, and suggests that hardness enhancement in Si-doped $WB_{4.2}$, like that in Zr-doped $WB_{4.2}$, is dominantly extrinsic/grain size induced in nature.

Table 2. Electron Density and Laplacians of BCPs at $B_{cluster}$-B_{layer} bonds (or $B_{cluster}$-C_{layer} in case of C dopant)

	Electron Density, au	Laplacian, au
Pure	0.115	-0.996
C	0.117	-0.156
Zr (edge)	0.114	-0.998
Zr (vertex)	0.107	-0.06

Conclusions

Tungsten tetraborides have been extensively explored due to their unique rigid pseudo-cage structures that result in high hardness. The partially occupied tungsten sites and voids in the crystal structure also make WB_4 of particular interest for enhancing hardness by doping heteroatoms into the WB_4 lattice. Because of this, extensive work has been carried out to enhance the hardness of

WB_4 by doping heteroatoms into the crystal lattice, modifying the overall composition of composite materials, and introducing/modifying grain boundaries. The challenge, exemplified in this work, is that very often, all of these processes occur simultaneously. As a result, it is difficult to develop a predictive understanding of the most effect ways to enhance hardness. In the current study, significant decreases in grain size were observed in all solid solutions, and, in parallel, the hardness was greatly enhanced. While the significant decrease of grain size in these solid solutions suggests extrinsic or grain-boundary based hardening effects, lattice specific strain analysis indicates that such a conclusion is not uniformly true in these materials. High-pressure studies, together with computational work, demonstrate significant change of bonding upon doping, in both the positive and negative directions. Specifically, doping carbon into WB_4 strengthens the bonding in the cage structure, resulting in better resistance to plastic deformation. In contrast, doping Zr and Si into WB_4 disrupts the cage structure, consequently leading to weaker intrinsic strength. For both Zr and Si, however, the reduced grain size and potential improved grain boundary strength compensates for the reduced bond strength, resulting in enhanced hardness, but a reduction in the plateau value of the differential strain. This work thus shows that through a combination of morphological studies, high-pressure diffraction experiments, and first-principles calculations, the hardening effects in a highly complex, multiphase material like doped WB_4 can be thoroughly understood from both intrinsic and extrinsic perspectives.

Experimental Procedure

Synthesis of WB_4 and solid solutions

Metal boride samples were synthesized by arc-melting stoichiometric amounts of metal and boron. The prepared phases were partly crushed into powder and analyzed by laboratory powder X-ray diffraction (PXRD) and partly encased into epoxy resin and polished. The polished samples were used for Vickers hardness micro-indentation, scanning electron microscopy (SEM) and energy-dispersive X-ray spectroscopy (EDS). Samples were further analyzed using nonhydrostatic *in situ* high-pressure radial X-ray diffraction performed in a diamond anvil cell at synchrotron beamline 12.2.2 of the Advanced Light Source (ALS, Lawrence Berkeley National Laboratory).

Alloys of WB_4 with carbon and silicon were prepared using: tungsten (99.95%, Strem Chemicals, U.S.A.), amorphous boron (99+%, Strem Chemicals, U.S.A.), tantalum (99.9%, Strem Chemicals, U.S.A.), silicon (99.9%, American Elements, U.S.A.), and tungsten carbide (99.5%, Strem Chemicals, U.S.A.). For these alloys the M:B ratio was kept at 1:4.5 and 1:11.6. For samples with a nominal composition of $(W_{1-x}C_x)$:4.5B, $(W_{0.67}Ta_{0.33})$:C_x:4.5B, x = 0.00, 0.02, 0.04, 0.06, 0.08, 0.10, 0.15, 0.20, 0.30, 0.40, 0.50; samples with a nominal composition of $(W_{1-z}C_z)$:11.6B, $(W_{0.92}Zr_{0.08})$:C_z:11.6B, z = 0.00, 0.02, 0.04, 0.05, 0.06, 0.08, 0.10, 0.20, 0.25, 0.30, 0.40, 0.50; and for samples with a nominal composition of $(W_{1-t}Si_t)$:4.5B, $(W_{1-t}Si_t)$:11.6B, t = 0.00, 0.02, 0.04, 0.06, 0.08, 0.10, 0.20, 0.25, 0.30, 0.40, 0.50.

Boron and metal powders in appropriate ratios were mixed in an agate mortar with a pestle to ensure homogeneity. A hydraulic press (Carver) was used to press the mixtures of powders into pellets with a diameter of 1.27 cm (0.5 in) under a 10-ton load. The pressed pellets were then placed into an arc-melting chamber on top of a water-cooled copper hearth. The chamber was then sealed and evacuated under vacuum for 20 minutes, followed by filling with argon; this was repeated at least 4 times. Before arc-melting the samples, getters made of titanium and zirconium were melted in order to “absorb” any trace oxygen and finally the samples were then arc melted

using I > 70 amps (typically 145 amps) for 1 - 2 min. The samples were heated until molten, flipped and re-arced at least 2 times to ensure homogeneity.

The prepared samples were separated into two halves using a diamond saw (Ameritool Inc., U.S.A.), with one half crushed into sub-40 μm powder for powder X-ray diffraction analysis (PXRD) using a Plattner-style crusher, while the other half was encapsulated into epoxy for scanning electron microscopy (SEM)/energy dispersion spectroscopy (EDS) and Vickers hardness testing using an epoxy/hardener set (Allied High Tech Products Inc., U.S.A.).

Characterization

In order to polish the samples to an optically flat surface, SiC papers (120 – 1200 grit sizes, Allied High Tech Products Inc., U.S.A.) and diamond films with particle sizes ranging from 30 to 1 micron (South Bay Technology Inc., U.S.A.) were used on a semi-automated polishing station (South Bay Technology Inc., U.S.A.).

To establish the purity and phase composition of the samples, PXRD and SEM techniques were used. PXRD was performed on a Bruker D8 Discover Powder X-ray Diffractometer (Bruker Corporation, Germany) using a Cu Kα X-ray beam (λ = 1.5418 Å) in the 5 - 100^{o} 2θ range with a step size of 0.0353^{o}, scan speed of 0.1055^{o}/sec and time per step of 0.3 sec. The Joint Committee on Powder Diffraction Standards (JCPDS) database was used to identify the phases present in the samples. *Maud* software was used to perform the unit cell refinements.[26–30] The phase purity was further verified on the polished samples using an UltraDry EDS detector (Thermo Scientific, U.S.A.) attached to a FEI Nova 230 high-resolution scanning electron microscope (FEI Company, U.S.A.).

Vickers hardness test

Hardness measurements were performed on polished samples using a load-cell type multi-Vickers hardness tester (Leco, U.S.A.) with a pyramidal diamond indenter tip. Under each applied load: 0.49, 0.98, 1.96, 2.94 and 4.9 N, 10 indents were made in randomly chosen spots on the sample surface. The lengths of the diagonals of the indents were measured using a high-resolution optical microscope, Zeiss Axiotech 100HD (Carl Zeiss Vision GmbH, Germany) with a 500x magnification. Vickers hardness values (H_v in GPa) were calculated using the following formula (Equation 1) and the values of all 10 indents per load were averaged:

$$H_v = \frac{1854.4F}{d^2} \quad (1)$$

where *d* is the arithmetic average length of the diagonals of each indent in microns and F is the applied load in Newtons (N).

High-Pressure experiment

Nonhydrostatic *in situ* high-pressure radial X-ray diffraction was performed in a diamond anvil cell at synchrotron beamline 12.2.2 of the Advanced Light Source (ALS, Lawrence Berkeley National Laboratory). Crushed powder of the samples ($W_{0.96}C_{0.04}$: 11.6 B and $W_{0.92}Zr_{0.08}$: 11.6 B) was loaded into a laser-drilled hole (~60 μm in diameter, ~60 μm in depth) in a ~400 μm diameter boron gasket made of amorphous boron and epoxy. Both samples adopt the WB_4 structure, therefore we abbreviate them as $W_{0.96}C_{0.04}B_4$ and $W_{0.92}Zr_{0.08}B_4$ when we mention these two samples in the text. A small piece of Pt foil (~20 μm diameter) was placed on top of the sample to serve as an internal pressure standard. A monochromatic X-ray beam (λ = 0.4959 Å, spot size = 30 μm × 30 μm) was passed through the sample, which was compressed between two diamond tips up to 60 GPa of pressure, and 2-D diffraction data were collected using an MAR-345 image plate and FIT2D software. A cerium dioxide (CeO_2) standard was used to calibrate the detector

distance and orientation. The stress state of the sample under nonhydrostatic compression was analyzed by Igor Pro (WaveMetrics, Inc.) based on lattice strain theory.

In the radial geometry, the X-rays are directed onto the sample through the boron gasket and between the diamond culets. The collected 2-dimensional diffraction patterns contain information on the d-spacings in the low and high stress directions, and at all intermediate angles. The stress in the sample under uniaxial compression is described by Equation (2):

$$\sigma = \begin{bmatrix} \sigma_1 & 0 & 0 \\ 0 & \sigma_1 & 0 \\ 0 & 0 & \sigma_3 \end{bmatrix} = \begin{bmatrix} \sigma_p & 0 & 0 \\ 0 & \sigma_p & 0 \\ 0 & 0 & \sigma_p \end{bmatrix} + \begin{bmatrix} -t/3 & 0 & 0 \\ 0 & -t/3 & 0 \\ 0 & 0 & -2t/3 \end{bmatrix} \quad (2)$$

where σ_1 is the minimum stress along the radial direction, σ_3 is the maximum stress in the axial direction, σ_P is the hydrostatic stress component, and t is the differential stress, which gives a lower-bound estimate of yield strength. Each line in the two-dimensional cake pattern corresponds to a d-spacing and starts as a straight line at low pressure, indicating a hydrostatic stress state. At high pressure, the lines deviate to lower angles in the low stress direction (σ_1) and to higher angles in the high stress direction (σ_3) (**FIG. S7-9**). The integrated one-dimensional diffraction pattern at the magic angle shifts to higher angles with increasing pressure, as the lattice spacing decreases upon compression (**FIG. S7-9**). The d-spacing is calculated by:

$$\mathrm{d_m(hkl)} = \mathrm{d_p(hkl)}[1 + (1 - 3\cos^2\varphi)\mathrm{Q(hkl)}] \quad (3)$$

where d_m is the measured d-spacing, d_p is the d-spacing under the hydrostatic component of the stress, φ is the angle between the diffraction normal and axial directions, and Q(hkl) is the lattice strain under the uniaxial stress condition. The differential stress, *t*, is directly related to the differential strain, *t(hkl)/G(hkl)*, by:

$$t(hkl) = 6G(hkl)Q(hkl) \quad (4)$$

where *G(hkl)* is the shear modulus of the specific lattice plane. The lattice parameters at each pressure calculated from the d-spacings at φ = 54.7° are summarized in **Table S1 & S2**. Incompressibility was then determined using the third order Birch-Murnaghan equation-of-state (EOS), which can be written as:

$$P = \frac{3}{2}K_0\left(\left(\frac{V_0}{V}\right)^{7/3} - \left(\frac{V_0}{V}\right)^{5/3}\right)\left(1 + \frac{3}{4}(K_0' - 4)\left(\left(\frac{V_0}{V}\right)^{2/3} - 1\right)\right) \quad (5)$$

where P is the pressure, K_0 is the bulk modulus, V is the volume, V_0 is the undeformed unit cell volume, and K_0' is the derivative of K_0 with respect to P.

Computation details

The sampling of the B_3-cluster distributions within a 3×2×1-supercell was performed with Site Disorder Occupancy.[31] All quantum mechanical calculations in this work were performed within the GGA PBE[32,33] functional, as implemented in VASP.[34–36] The kinetic energy cutoff of 750 eV together with the 2nd order Methfessel-Paxton approximation with $\sigma = 0.2$ were used. The first Brillouin zone was sampled using Gamma-centered Monkhorst-Pack Grids with k-point mesh density of $2\pi \times 0.025\text{Å}^{-1}$. All structures were relaxed until the forces on each atom were ≤0.01 eV.

Quantum Theory of Atoms and Molecules (QTAIM) calculations were performed using Critic2 software.[37,38] A recursive subdivision of the Wigner-Seitz cell algorithm was used to locate critical points such that the Morse number of the resulting graph equals to zero. The integration of atomic basins for Bader charge calculations the Yu and Trinkle (YT)[39] method was utilized. QTAIM is a method to analyze the topology of the electron density, $\rho(\vec{r})$. In QTAIM, each atom is associated with a nuclear critical point (NCP) — a local maximum in $\rho(\vec{r})$, and an atomic basin — a portion of space surrounded by a zero-flux surface ($\nabla\rho(\vec{r})$). A Bader charge of an atom is the

difference between the number of valence electrons and integral of $\rho(\vec{r})$ within the atomic basin. $\rho(\vec{r})$ contains four types of critical points: nuclear critical points (NCP) have three negative eigenvalues of the Hessian (local maxima); bond critical points (BCP) have two negative and one positive eigenvalues of the Hessian (saddle points); ring critical point (RCP) have one positive and two negative eigenvalues of the Hessian (second order saddle points); cage critical points (CCP) have three positive eigenvalues of the Hessian (local minima). Paths that trace the direction of maximum gradient of $\rho(\vec{r})$ between two NCPs are called bond paths, defining a bond. A point of the intersection of a bond path and an atomic basin surface is a BCP, and it determines the properties of the bond. In this work, we used the electron density, $\rho(\vec{r})$, at a BCP (linked with the occupation of the bond, and the bond strength for metallic systems), and the Laplacian of electron density, $\nabla\rho(\vec{r})$, at a BCP (associated with the electron depletion: the more negative $\nabla\rho(\vec{r})$ — the more stable the bond is).

Acknowledgments

The authors thank M. Kunz, B. Kalkan and K. Armstrong for technical support at the Lawrence Berkeley National Laboratory (LBNL) beamline 12.2.2. This work was financially supported by the National Science Foundation Division of Materials Research under grant DMR-2312942 (R.B.K. and S.H.T.). DFT studies have been supported by the NSF CHE- 2203366 grant to A.N.A. Radial diffraction experiments were performed at the Advanced Light Source at Lawrence Berkely National Laboratory at Beamline 12.2.2. Beamline 12.2.2 at the Advanced Light Source is a DOE Office of Science User Facility supported under contract no. DE-AC02-05CH11231. This research was partially supported by COMPRES, the Consortium for Materials Properties Research in Earth Sciences under NSF Cooperative Agreement EAR 1606856.

Supporting Information

Tabulated lattice parameters of WCB_4 and $WZrB_4$. XRD patterns and SEM images for all $(W_{0.67}Ta_{0.33})C_x$:4.5B and $(W_{0.92}Ta_{0.08})C_x$:4.5B samples. Vickers hardness for all concentrations of $(W_{1-x}C_x)$:4.5B, $(W_{1-x}Si_x)$:4.5B, $(W_{0.67}Ta_{0.33})C_x$:4.5B and $(W_{0.92}Ta_{0.08})C_x$:4.5B samples. Representative synchrotron X-ray diffraction patterns for WCB_4, $WZrB_4$ and $WSiB_4$. Differential strain of additional lattice places (101, 110) for WB_4, $WZrB_4$, WCB_4 and $WSiB_4$. Ensemble of $3\times2\times1$-supercell $WB_{4.2}$ realizations.

References

1. Akopov, G., Yeung, M. T. M. T. & Kaner, R. B. R. B. Rediscovering the Crystal Chemistry of Borides. *Adv. Mater.* **29**, 1604506 (2017).
2. Fokwa, B. P. T. Borides: Solid-State Chemistry. *Encycl. Inorg. Bioinorg. Chem.* 1–14 (2014) doi:10.1002/9781119951438.eibc0022.pub2.
3. Samsonov, G. V., Markovskii, L. Ya., Zhigach, A. F. & Valyashko, M. G. *Boron, Its Compounds and Alloys [in Russian]*. (House of the Academy of the Sciences Ukrainian SSR, 1960).

4. Samsonov, G. V., Serebriakova, T. I. & Neronov, V. A. *Borides [in Russian]*. (Atomizdat, 1975).
5. Samsonov, G. V. & Vinitskii, I. M. *Refractory compounds [in Russian]*. (Atomizdat, 1975).
6. Buschow, K. H. J. Magnetic Properties of Borides. in *Boron and Refractory Borides* (ed. Matkovich, V. I.) 494–515 (Springer Berlin Heidelberg, 1977). doi:10.1007/978-3-642-66620-9_26.
7. Scheifers, J. P., Zhang, Y. & Fokwa, B. P. T. Boron: Enabling Exciting Metal-Rich Structures and Magnetic Properties. *Acc. Chem. Res.* **50**, 2317–2325 (2017).
8. Chung, H.-Y. *et al.* Synthesis of Ultra-Incompressible Superhard Rhenium Diboride at Ambient Pressure. *Science* **316**, 436–439 (2007).
9. Chung, H.-Y. *et al.* Response to Comment on 'Synthesis of Ultra-Incompressible Superhard Rhenium Diboride at Ambient Pressure'. *Science* **318**, 1550 (2007).
10. Mohammadi, R. *et al.* Tungsten tetraboride, an inexpensive superhard material. *Proc. Natl. Acad. Sci.* **108**, 10958–10962 (2011).
11. Yeung, M. T. *et al.* Superhard Monoborides: Hardness Enhancement through Alloying in W1−xTaxB. *Adv. Mater.* **28**, 6993–6998 (2016).
12. Yeung, M. T. *et al.* Superhard W0.5Ta0.5B nanowires prepared at ambient pressure. *Appl. Phys. Lett.* **109**, (2016).
13. Mohammadi, R. *et al.* Enhancing the Hardness of Superhard Transition-Metal Borides: Molybdenum-Doped Tungsten Tetraboride. *Chem. Mater.* **28**, 632–637 (2016).
14. Akopov, G., Yeung, M. T., Turner, C. L., Mohammadi, R. & Kaner, R. B. Extrinsic hardening of superhard tungsten tetraboride alloys with group 4 transition metals. *J. Am. Chem. Soc.* **138**, 5714–5721 (2016).
15. Xie, M. *et al.* Exploring hardness enhancement in superhard tungsten tetraboride-based solid solutions using radial X-ray diffraction. *Appl. Phys. Lett.* **107**, 41903 (2015).

16. Mohammadi, R. *et al.* Toward Inexpensive Superhard Materials: Tungsten Tetraboride-Based Solid Solutions. *J. Am. Chem. Soc.* **134**, 20660–20668 (2012).
17. Akopov, G. *et al.* Effects of Dodecaboride-Forming Metals on the Properties of Superhard Tungsten Tetraboride. *Chem. Mater.* **30**, (2018).
18. Akopov, G. *et al.* Effects of Variable Boron Concentration on the Properties of Superhard Tungsten Tetraboride. *J. Am. Chem. Soc.* **139**, 17120–17127 (2017).
19. Akopov, G., Sobell, Z. C., Yeung, M. T. & Kaner, R. B. Stabilization of LnB12 (Ln = Gd, Sm, Nd, and Pr) in Zr(1– x)Ln(x)B12 under Ambient Pressure. *Inorg. Chem.* **55**, 12419–12426 (2016).
20. Akopov, G., Roh, I., Sobell, Z. C., Yeung, M. T. M. T. & Kaner, R. B. R. B. Investigation of ternary metal dodecaborides (M1M2M3)B12 (M1, M2 and M3 = Zr, Y, Hf and Gd). *Dalton Trans* **47**, 6683–6691 (2018).
21. Akopov, G., Yeung, M. T., Turner, C. L., Li, R. L. & Kaner, R. B. Stabilization of HfB12 in Y1-xHfxB12 under Ambient Pressure. *Inorg. Chem.* **55**, (2016).
22. Akopov, G. *et al.* Superhard mixed transition metal dodecaborides. *Chem. Mater.* **28**, 6605–6612 (2016).
23. Akopov, G., Yin, H., Roh, I., Pangilinan, L. E. & Kaner, R. B. Investigation of Hardness of Ternary Borides of the YCrB4, Y2ReB6, Y3ReB7, and YMo3B7 Structural Types. *Chem. Mater.* **30**, (2018).
24. Akopov, G., Pangilinan, L. E. L. E., Mohammadi, R. & Kaner, R. B. R. B. Superhard metal borides: A look forward. *APL Mater.* **6**, 070901 (2018).
25. Portnoi, K. I. I. *et al.* Phase diagram of the system tungsten-Boron. *Sov. Powder Metall. Met. Ceram.* **6**, 398–402 (1967).
26. Lutterotti, L., Chateigner, D., Ferrari, S. & Ricote, J. Texture, residual stress and structural analysis of thin films using a combined X-ray analysis. *Thin Solid Films* **450**, 34–41 (2004).

27. Lutterotti, L., Bortolotti, M., Ischia, G., Lonardelli, I. & Wenk, H. R. Rietveld texture analysis from diffraction images. *Z. Krist. Suppl.* **1**, 125–130 (2007).
28. Lutterotti, L. Maud Rev. 2.55. *Univ. Trento-Italy Dep. Ind. Eng. Trento Italy* (2015).
29. Lutterotti, L. Total pattern fitting for the combined size-strain-stress-texture determination in thin film diffraction. *Nucl. Instrum. Methods Phys. Res. Sect. B Beam Interact. Mater. At.* **268**, 334–340 (2010).
30. Lutterotti, L., Matthies, S., Wenk, H. R., Schultz, A. S. & Richardson, J. W. Combined texture and structure analysis of deformed limestone from time-of-flight neutron diffraction spectra. *J. Appl. Phys.* **81**, 594–600 (1997).
31. Grau-Crespo, R., Hamad, S., Catlow, C. R. A. & Leeuw, N. H. de. Symmetry-adapted configurational modelling of fractional site occupancy in solids. *J. Phys. Condens. Matter* **19**, 256201 (2007).
32. Perdew, J. P., Burke, K. & Ernzerhof, M. Generalized Gradient Approximation Made Simple. *Phys. Rev. Lett.* **77**, 3865–3868 (1996).
33. Perdew, J. P., Burke, K. & Ernzerhof, M. Generalized Gradient Approximation Made Simple [Phys. Rev. Lett. 77, 3865 (1996)]. *Phys. Rev. Lett.* **78**, 1396–1396 (1997).
34. Kresse, G. & Furthmüller, J. Efficiency of ab-initio total energy calculations for metals and semiconductors using a plane-wave basis set. *Comput. Mater. Sci.* **6**, 15–50 (1996).
35. Kresse, G. & Hafner, J. Ab initio molecular-dynamics simulation of the liquid-metal--amorphous-semiconductor transition in germanium. *Phys. Rev. B* **49**, 14251–14269 (1994).
36. Kresse, G. & Hafner, J. Ab initio molecular dynamics for liquid metals. *Phys. Rev. B* **47**, 558–561 (1993).
37. Otero-de-la-Roza, A., Blanco, M. A., Martín Pendás, A. & Luaña, V. Critic: a new program for the topological analysis of solid-state electron densities. *Comput. Phys. Commun.* **180**, 157–166 (2009).

38. Otero-de-la-Roza, A., Johnson, E. R. & Luaña, V. Critic2: A program for real-space analysis of quantum chemical interactions in solids. *Comput. Phys. Commun.* **185**, 1007–1018 (2014).
39. Yu, M. & Trinkle, D. R. Accurate and efficient algorithm for Bader charge integration. *J. Chem. Phys.* **134**, 064111 (2011).
40. Perdew, J. P., Burke, K. & Ernzerhof, M. Generalized Gradient Approximation Made Simple (vol 77, pg 3865, 1996). *Phys. Rev. Lett.* **78**, 1396–1396 (1997).
41. Perdew, J. P., Burke, K. & Ernzerhof, M. Generalized gradient approximation made simple. *Phys. Rev. Lett.* **77**, 3865–3868 (1996).
42. Kresse, G. & Furthmüller, J. Efficient iterative schemes for ab initio total-energy calculations using a plane-wave basis set. *Phys. Rev. B - Condens. Matter Mater. Phys.* **54**, 11169–11186 (1996).
43. Kresse, G. & Furthmüller, J. Efficiency of ab-initio total energy calculations for metals and semiconductors using a plane-wave basis set. *Comput. Mater. Sci.* **6**, 15–50 (1996).
44. Kresse, G. & Hafner, J. Ab initio molecular dynamics for liquid metals. *Phys. Rev. B* **47**, 558–561 (1993).
45. Kresse, G. & Hafner, J. Ab initio molecular-dynamics simulation of the liquid-metalamorphous-semiconductor transition in germanium. *Phys. Rev. B* **49**, 14251–14269 (1994).
46. Grau-Crespo, R., Hamad, S., Catlow, C. R. A. A., De Leeuw, N. H. & de Leeuw, N. H. Symmetry-adapted configurational modelling of fractional site occupancy in solids. *J. Phys. Condens. Matter* **19**, 256201 (2007).
47. Otero-de-la-Roza, A., Blanco, M. A., Pendás, A. M. & Luaña, V. Critic: a new program for the topological analysis of solid-state electron densities. *Comput. Phys. Commun.* **180**, 157–166 (2009).
48. Otero-de-la-Roza, A., Johnson, E. R. & Luaña, V. Critic2: A program for real-space analysis of quantum chemical interactions in solids. *Comput. Phys. Commun.* **185**, 1007–1018 (2014).

49. Bodrova, L. G., Koval'chenko, M. S. & Serebryakova, T. I. Preparation of tungsten tetraboride. *Sov. Powder Metall. Met. Ceram.* **13**, 1–3 (1974).

50. Samsonov, G. V. The Phases of the Tungsten-Boron System. *Dokl Akad Nauk SSSR* **113**, 1299–1301 (1957).

51. Lech, A. T., Turner, C. L., Mohammadi, R., Tolbert, S. H. & Kaner, R. B. Structure of superhard tungsten tetraboride: A missing link between MB2 and MB12 higher borides. *Proc. Natl. Acad. Sci.* **112**, 3223–3228 (2015).

52. Akopov, G. *et al.* Synthesis and Characterization of Single-Phase Metal Dodecaboride Solid Solutions: Zr1–xYxB12 and Zr1–xUxB12. *J. Am. Chem. Soc.* **141**, 9047–9062 (2019).

53. McCaughey, C. & Tsakiropoulos, P. Type of primary Nb5Si3and precipitation of Nbssin αNb5Si3in a Nb-8.3Ti-21.1Si-5.4Mo-4W-0.7Hf (at.%) near eutectic Nb-silicide-based alloy. *Materials* **11**, 1–25 (2018).

54. Lei, J. *et al.* Radial X-Ray Diffraction Study of Superhard Early Transition Metal Dodecaborides under High Pressure. *Adv. Funct. Mater.* **29**, 1900293 (2019).

55. Xie, M. *et al.* Exploring the high-pressure behavior of superhard tungsten tetraboride. *Phys. Rev. B* **85**, 064118 (2012).

56. Råasander, M. & Moram, M. A. On the accuracy of commonly used density functional approximations in determining the elastic constants of insulators and semiconductors. *J. Chem. Phys.* **143**, 144104 (2015).

57. Heyd, J., Scuseria, G. E. & Ernzerhof, M. Hybrid functionals based on a screened Coulomb potential. *J. Chem. Phys.* **118**, 8207–8215 (2003).

58. Heyd, J., Scuseria, G. E. & Ernzerhof, M. Erratum: "Hybrid functionals based on a screened Coulomb potential" [J. Chem. Phys. 118, 8207 (2003)]. *J. Chem. Phys.* **124**, 219906 (2006).